Journal of Micro- and Nano-Manufacturing. Received June 07, 2018;
Accepted manuscript posted October 10, 2018. doi:10.1115/1.4041668


# NANOPARTICLE SINTERING MODEL, SIMULATION AND CALIBRATION AGAINST EXPERIMENTAL DATA

**Obehi G Dibua**
University of Texas at Austin
Department of Mechanical Engineering
Austin, TX, USA
email: ogodibua@utexas.edu

**Anil Yuksel**
University of Texas at Austin
Department of Mechanical Engineering
Austin, TX, USA
email: anil.yuksel@utexas.edu

**Nilabh K Roy**
University of Texas at Austin
Department of Mechanical Engineering
Austin, TX, USA
email: nilabh.roy@utexas.edu

**Chee S Foong**
NXP Semiconductors
Austin, TX, USA
email: cs.foong@nxp.com

**Michael Cullinan**
University of Texas at Austin
Department of Mechanical Engineering
Austin, TX, USA
email: michael.cullinan@austin.utexas.edu



## ABSTRACT

One of the limitations of commercially available metal additive manufacturing (AM) processes is the minimum feature size most processes can achieve. A proposed solution to bridge this gap is microscale selective laser sintering (μ-SLS). The advent of this process creates a need for models which are able to predict the structural properties of sintered parts. While there are currently a number of good SLS models, the majority of these models predict sintering as a melting process which is accurate for microparticles. However, when particles tend to the nanoscale, sintering becomes a diffusion process dominated by grain boundary and surface diffusion between particles. As such, this paper presents an approach to model sintering by tracking the diffusion between nanoparticles on a bed scale. Phase Field Modeling (PFM) is used in this study to track the evolution of particles undergoing sintering. Changes in relative density are then calculated from the results of the PFM simulations. These results are compared to experimental data obtained from furnace heating done on dried copper nanoparticle inks, and the simulation constants are calibrated to match physical properties.

## INTRODUCTION

The resolution of currently available metal additive manufacturing (AM) technologies is generally on the order of hundreds of micrometers [1,2]. This resolution prevents AM technologies from expanding into industries, such as the microelectronics industry, where sub-10 μm part sizes are critical. Parts fabricated for the microelectronics industry are typically made using a combination of lithography, etching and material deposition processes to create 2.5D electronic structures. However, there are size limitations and associated complexities with using these processes. The need for a more flexible manufacturing process which matches the desired tolerances needed for creating 3D microelectronic structures is being filled through the creation of a microscale selective laser sintering process (μ-SLS) [3-5].

Selective Laser Sintering (SLS) is an AM process by which parts are created through the fusion of particles using energy absorbed from a laser source. In the traditional SLS process, powder is spread onto a bed and a laser beam is rastered over the powder bed, providing the particles heated by the laser with enough heat energy to fuse together and form a solid part [6]. This process is different from other AM processes, in that it is powder based and uses a laser as the heat source. The powder base allows for the creation of features like overhangs as sintered parts are supported by unsintered powder underneath it. Micro-SLS differs from the traditional SLS process in that it deals with the sintering of nanoparticles, which would allow for smaller features and microscale resolution. With the creation of this new technology, there is an associated need for models able to predict the final properties of sintered parts.

There are currently a number of good SLS models [7-9], but these models deal with microparticles and as such model sintering as a melting process. During the

sintering of nanoparticles, the mechanism behind sintering becomes dominated by nanoscale effects. Some of these effects include, but are not limited to, vapor, volume, grain boundary and surface diffusion, viscous flow, and grain-boundary sliding/dislocations [10]. The particles used for this study are on the order of ten to a hundred nanometers. For this size of particles, the dominant means of sintering has been shown to be surface and grain-boundary diffusion [10]. Consequently, the simulations presented in this paper model sintering as a diffusion process dominated by surface and grain boundary diffusion, with minimal volume diffusion contributions.

## BACKGROUND

Studying sintering as a diffusion process is not a novel idea. A number of simulations study sintering as a diffusion driven process. Ding and Pan studied the sintering between nanoparticles using molecular dynamics (MD) simulations which track the atomistic interactions between particles [11]. These MD simulations made use of the Lennard-Jones model to track the potential between particles. Because MD simulations track the interactions between atoms, these simulations are only able to model a few particles at a time. Ding and Pan also compared continuum and MD models for the sintering of nanoparticles. This comparison led to the realization that the preliminary assumptions required for continuum models made them inadequate for tracking the sintering kinetics which change during the MD simulations. Cheng and Ngan were able to expand from the few particle MD simulations to tracking four particles, broken into half, quarter and octet portions and arranged in an FCC crystalline state [12]. Though these MD models are able to track all phases of the sintering process, they have the disadvantage of being too computationally expensive to track more than a few particles at a time. Alternative to these MD models, there are discrete models which are able to track particles on a bed scale. Rojek et al modelled sintering as a diffusion process using a Discrete Element Method (DEM) [13]. They found shrinkage between particles to be driven by inter-particle attraction which is caused by the stresses and surface tension in the necks formed between particles. Though this model was able to monitor a large number of particles, sintering is modeled as a bulk process which is governed by a particle interaction model dependent on only grain boundary diffusion. The downside with discrete models is that they are unable to model nanoscale effects during sintering. Thus the gap exists between the MD models which characterize full nanoscale effects but can only model a few particles at a time and the discrete models which model full beds but are unable to model nanoscale effects. Phase Field Modelling (PFM) can bridge this gap.

A number of Phase Field models have been created to track the sintering behavior between particles. Wang used PFM to track the sintering between 26 particles [14] and Shinagawa used a combination of PFM and DEM to track the sintering between a cluster made up of 10 particles [15]. With both of these models, the sintering behavior is successfully characterized for the particles in 2D. While 2D simulations provide useful insight into the process of diffusion between particles, they cannot accurately be used to predict properties of real particle beds such as volumetric shrinkage. Kumar used PFM to track the sintering of 28 3D particles randomly arranged in a cubic lattice [16].

In contrast to the previously mentioned models, the simulation used in this study is able to track the sintering between hundreds of particles. This study simulates sintering in a 43 particle one-by-one micron bed and a 134 particle two-by-two micron bed. Additionally, a data analysis package is created to determine the change in density of the bed. The relative density of the beds are plotted as functions of simulation time and compared against similar results from experimental data. This comparison is used to calibrate the simulation constants, mapping simulation results to physical experiments.

## MODEL

A Phase Field Model (PFM) was used in this study to track the sintering of particles. PFM is a diffuse-interface approach which tracks the evolution of particles using phase field variables which are related to microscopic parameters [17]. In this study, the PFM variables used are the conserved mass density ($\rho$) variable and the non-conserved order parameter ($\eta_i$). These variables take on values from 0 to 1 tracking the phases of, and interphases between, particles. The density variable differentiates between solid phase, where it takes the value of 1, and the vapor phase, where it takes the value of 0. On the other hand, the order parameter takes on the value of 1 for the ith particle and is 0 for every other particle. The evolution of particles in this system is driven by the

Journal of Micro- and Nano-Manufacturing. Received June 07, 2018;
Accepted manuscript posted October 10, 2018. doi:10.1115/1.4041668


minimization of the total free energy, which is a function of the phase field variables and is given in Eq. 1.

$$F = \int_V \left[ f(\rho,\eta_i) + \frac{1}{2}\beta_\rho |\nabla\rho|^2 + \frac{1}{2}\sum_{i=1}^{N} \beta_\eta |\nabla\eta_i|^2 \right] dV \quad (1)$$

$f(\rho,\eta_i)$ is the bulk free energy, $N$ is the total number of particles in the system, $\beta_\rho$ is the gradient energy term for the density variable, and $\beta_\eta$ is the gradient energy term for the order parameter. The bulk free energy is a Landau type potential shown in Eq. 2. [16].

$$\begin{aligned} f(\rho,\eta_i) &= K_1\left(\rho^4 + \frac{-4\rho_{vap} - 4\rho_{sol} - 2}{3}\rho^3 + \frac{4\rho_{vap}\rho_{sol} + 2\rho_{vap} + 2\rho_{sol}}{2}\rho^2 - 2\rho_{vap}\rho_{sol}\rho\right) \\ &+ K_2\left(\rho^2 + 6(1-\rho)\sum_{i=1}^{N}{\eta_i}^2 - 4(2-\rho)\sum_{i=1}^{N}{\eta_i}^3 + 3\sum_{i=1}^{N}{\eta_i}^4 + w\sum_{i=1}^{N}\sum_{j=1,j\neq i}^{N}{\eta_i}^2{\eta_j}^2\right) \end{aligned} \quad (2)$$

where $\rho_{vap}$ and $\rho_{sol}$ are the vapor and solid density parameters respectively, $w$ is related to the grain boundary energy, K1 and K2 are constants related to grain boundary and surface energy as shown in Eqs 3 and 4. In addition to K1 and K2, the gradient energy terms for the density variable and the order parameter, from Eq. 1, are related to the surface energy and grain boundary energy in the system. Chockalingam et al [18], showed that the surface and grain boundary energy are functions of the constants in Eq. 1 and Eq. 2. The relationship between these constants and the energy terms are shown in Eqs. 3 and 4.

$$\gamma_{gb} = \frac{2\sqrt{K_2\beta_\eta}}{\sqrt{3}} \quad (3)$$

$$\gamma_s = \frac{\sqrt{2\left(\beta_\rho + \beta_\eta\right)(K_1 + 7K_2)}}{6} \quad (4)$$

$\gamma_{gb}$ in Eq. 3 is the grain boundary energy and $\gamma_s$ in Eq. 4 is the surface energy. As stated earlier, the sintering kinetics is driven by the progression of the phase field variables. The temporal evolution of the density variable is governed by the Cahn-Hilliard equation [19,20] which is shown in Eq. 5.

$$\frac{\partial\rho}{\partial t} = \nabla.\left(D\nabla\frac{\delta F}{\delta\rho}\right) = \nabla.\left(D\nabla\left[\frac{\partial f(\rho,\eta_i)}{\partial\rho} - \beta_\rho\nabla^2\rho\right]\right) \quad (5)$$

$D$ is the equivalent diffusion coefficient, made up of fractions of the surface, grain boundary and volume diffusion coefficients, and is given by Eq. 6.

$$D = D_{vol}\emptyset + D_{surf}\rho^2(1-\rho^2) + D_{gb}\rho\left(1 - \sum_{i=1}^{N}{\eta_i}^2\right) \quad (6)$$

$D_{vol}$ is the volume diffusion coefficient, $D_{surf}$ is the surface diffusion coefficient, $D_{gb}$ is the grain boundary diffusion coefficient, and $\emptyset = \rho^4(7\rho^2 - 18\rho + 12)$ having a maximum in the solid phase and a minimum in the vapor phase [16]. The temporal evolution of the order parameter is governed by the time-dependent Ginzburg-Landau structural relaxation equation [21], given in Eq. 7 where L is a constant that characterizes grain boundary mobility.

$$\frac{\partial\eta_i}{\partial t} = -L\frac{\partial F}{\partial\eta_i} = -L\left(\frac{\partial f}{\partial\eta_i} - \beta_\eta\nabla^2\eta_i\right) \quad (7)$$

## SIMULATION

*Setup*

The equations for the field variables listed above were discretized using the Forward Euler method for numerical differentiation. These equations were encoded into a simulation using programming with C++, working in units of pixel length and simulation timesteps. Message Passing Interface (MPI) was then used in C++ to break the simulation box into different smaller boxes that could be analyzed by different processors. This parallel program was then run in a cluster using varying number of cores, depending on the size of the simulation box. The numerical data output from the C++ simulation is put into a python algorithm which plots the geometry of the bed, by converting the numerical data to the matching x-y-z

locations of pixels, with weights relating to the density and order parameter field variables. The constants used in the simulation correlate to sintering at different temperatures. For the initial test of the simulation, the constants used are $\beta\rho = 10$, $\beta\eta = 3.75$ in Eq. 1, K1 = 12, K2 = 1, w = 7 in Eq. 2, in Eq. 4 Dsurf = 45, Dgb = 4.1, Dvol = 0.08 and L = 10 in Eq. 5 [15]. These constants were arbitrarily chosen to correspond to a 10:1 ratio of surface to grain boundary diffusion and a 2:1 ratio of surface to grain boundary energy, derived from Equations 3 and 4. The value for the density in vapor phase ($\rho_{vap}$) was taken to be 0.000000089 and in solid phase ($\rho_{sol}$) 0.9998. These values were chosen instead of the standard values of 0 and 1, to allow for numerical analysis of the discretized differential equations. The simulation was initialized by setting pixels outside of a particle to $\rho_{vap}$ and in the particle to $\rho_{sol}$. The simulation takes in beds generated with a bed generation simulation and starts with the particles in contact.

*Bed Generation*

The bed generation tool used generates particles arranged to match an actual physical bed. These beds consist of spherical nanoparticles, generated by setting an initial position vector for each particle as well as a radius, to set particle size. The generation simulation uses Discrete Element Modelling (DEM), in a Multiphase Computational Fluid Dynamics simulation, MFIX. Particle packings are generated using the MFIX-DEM discrete mass inlet function, which allows each particle to interact with neighboring particles. Initially, the particles are distributed randomly within the bed domain, they are given an initial velocity and are allowed to move within an initial set of boundary conditions. Particle interactions are modeled using a dashpot model based on a soft-sphere model of the particles. Subject to gravitational and cohesive forces, the particles move around and interact until the final steady state position is reached. This final geometry is used as the input into the PFM simulation. Complete details of the bed generation process can be found in reference [22].

## RESULTS AND DISCUSSION

A number of procedures were done to test the capability and validity of the simulation described above. These procedures include running the simulation on a one-by-one and two-by-two micrometer bed to prove first, that the simulation works and produces results which are similar to experiments, and secondly that the simulation can be expanded for over a hundred particles. The results of these tests are discussed in more detail below.

*One-by-One Micrometer Bed*

A one-by-one micrometer bed was generated with the bed generation tool described earlier and is shown in Fig 1. This bed is made up of 43 particles in a simulation box with dimensions of 110 by 110 pixels in the x-y plane and 73 pixels in the z. This corresponds to a bed height of 750 nm and particles with diameters ranging from 146 to 573 nm with a mean of 218 nm, using a conversion factor of approximately 10.6 nm/pixel. The size range of this bed is designed to match the size distribution of the copper nanoparticles in the ink used for the experiments. The size distribution of this ink was derived from experiments to match a lognormal distribution with a mean of 232 nm and a standard deviation of 96 nm. Using a 64 core cluster, this simulation took approximately 19 hours to run to 2.4 million time steps. The results of the sintering simulation are shown in Fig. 1.

At the start of the sintering process particles are in contact to initiate diffusion. The average overlap between the particles at the start of the simulation is 0.0004 nm. At the initiation of sintering, necks begin to form between particles. These necks grow until the onset of coarsening where the boundary between particles migrates into the smaller particles shifting the balance of mass towards the larger particle. As shown in Fig. 1 the initial sintering periods are characterized by fast neck growth evident in images 1a – d. The neck formation happens rapidly leading to a faster looking rate of evolution than in the later time steps. The shrinkage and densification become clearer in the later images 1f – i as the pores prevalent in the previous time steps are filled due to diffusion as sintering occurs. The bed shown in Fig. 1 was simulated under isothermal conditions, with each particle having the same values for the diffusion and energy constants. The values in the description of Fig. 1 are the simulation timesteps and in parenthesis the amount of wall clock time it takes to get to the corresponding timestep.

Journal of Micro- and Nano-Manufacturing. Received June 07, 2018;
Accepted manuscript posted October 10, 2018. doi:10.1115/1.4041668


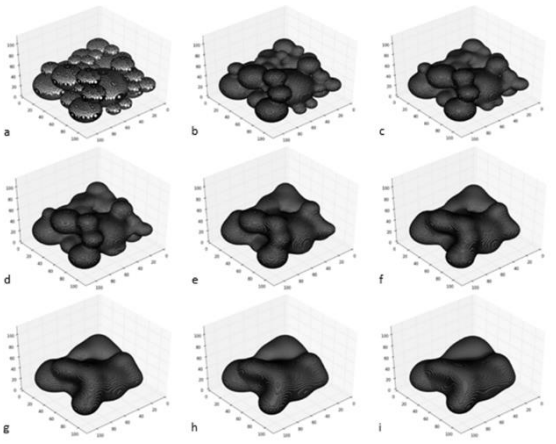


Fig. 1. The evolution of a one by one micrometer bed with 43 particles. a. Initial. b. 20000 timesteps (.16 hrs.) c. 60000 timesteps (.47 hrs.) d. 100000 timesteps (.79 hrs.); e. 280000 timesteps (2.2 hrs.) f. 450000 timesteps (3.6 hrs.) g. 700000 timesteps (5.5 hrs.) h. 850000 timesteps (6.7 hrs.) i. 1100000 timesteps (8.7 hrs.)

*Data Analysis*

Upon completion of the sintering simulation, the data collected from these simulations was analyzed to determine the change in relative density of the simulation over time. The density of the bed was found from analysis done on a 40-by-40 pixel box, which corresponds to a 423-by-423 nm box, in the center of the simulation bed. The PFM simulations assume that sintering occurs with particles that are surrounded by air, which allows for shrinkage across the x-y bounds of the simulation. As such, the analysis is done in the center of the simulation to ensure that the results collated are impervious to edge effects. In this analysis box, the calculations for density were found by taking the ratio of the total sum of the conserved density variable in the box, to the total volume of that box. With this method, the relative density has a value of 0 in a fully porous box and a value of 1 when fully dense. A cross-sectional view of the simulation box showing the inner box undergoing sintering is shown in Fig. 2.

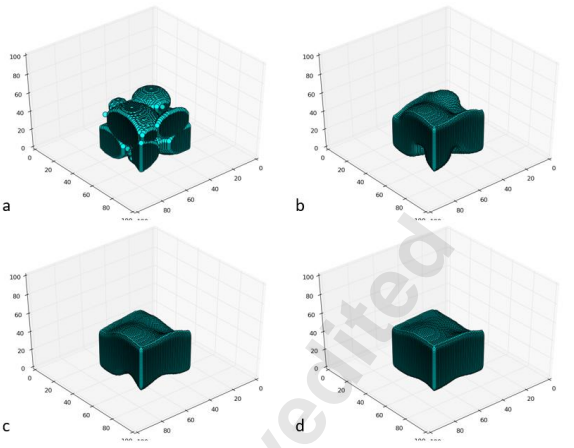


Fig. 2. Densification in the center of the simulation bed after a. 0 timesteps. b. 80000 timesteps. c. 160000 timesteps. d. 480000 timesteps

To get an uncertainty measure for the analysis done on these beds, several boxes were taken from each bed. These boxes were chosen based off an edge finding algorithm which gives the largest possible bounds for analysis without encroaching upon the edges of the simulation. The significance of this tool is the ability to determine the cutoff point between the fully populated bulk of the bed and the edges of the simulation which undergo x-y shrinkage. The edge finding algorithm works by taking strips of the full z height, along each slice in the x and y direction. In each z-strip the deviation from the top and bottom of the bed is calculated, and the total deviation is defined as the Euclidean norm of these values. The total deviation is then normalized against the largest difference in deviations for each bed. This gives the τ value found for the algorithm and is shown in Eq. 8 below.

$$\tau_i = \frac{\sqrt{\left({t_{D,i}}^2 + {b_{D,i}}^2\right)}}{max\left[\sqrt{\left({t_D}^2 + {b_D}^2\right)}\right] - min\left[\sqrt{\left({t_D}^2 + {b_D}^2\right)}\right]} \quad (8)$$

where $t_D$ and $b_D$ refer to the deviation of the z strip from the top and bottom of the bed respectively. Once τ is calculated, the algorithm compares this value to a predetermined cut off factor and defines the analysis bounds as the x and y values that give τ values just below the cut off. The optimum cut off factor for the simulation was determined analytically by varying

Journal of Micro- and Nano-Manufacturing. Received June 07, 2018;
Accepted manuscript posted October 10, 2018. doi:10.1115/1.4041668


different factor values to get the best agreement for all beds tested. Fig. 3 shows the average rate of relative density for a single one-by-one bed simulation run, as well as the associated error bounds calculated from varying the position of the analysis box. The relative density is defined in Eq. 9.

$$\rho_{rel} = \frac{\rho_i - \rho_o}{\rho_i} \tag{9}$$

Where $\rho_o$ is the sum of the density variable at the start of the simulation, and $\rho_i$ is the sum at the simulation timestep i.

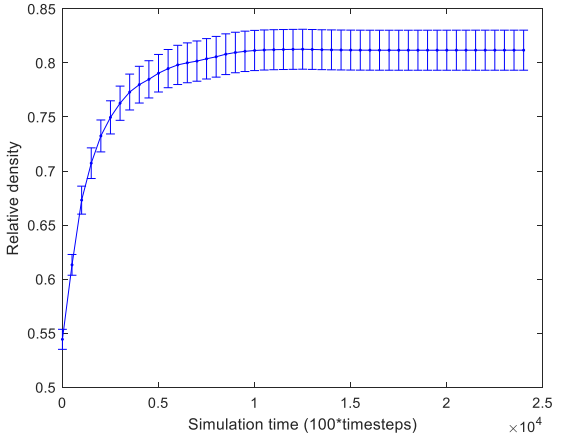


Fig. 3. Relative density curve, with error bounds, derived from data analysis done on the sintering simulation

*Experimental Procedure*

Once data analysis was done on the simulation beds, experiments were performed to validate the simulation results and calibrate the simulation constants to match physical properties. Specifically, the simulation time step was calibrated to match the sintering experiment time in minutes, and the simulation energy and diffusion constants were calibrated to match sintering temperatures. The experiments were carried out in a furnace using Intrinsiq CI-005 copper nanoparticle inks [23]. 2ml of copper nanoparticle ink was dispensed into a glass petri dish using a rubber pipette. The petri dish of ink was dried on a hot plate at around 95˚C for 16 hours. After the solvent in the ink was dried off, dried copper flakes of coated nanoparticles were scraped off the petri dish with a flat spatula. These dried flakes were then put into crucibles. Pressure was applied to form the flakes into pellets in the crucibles. These crucibles were put into a furnace and subject to isothermal heating. In the furnace, the coating around the particles dried off and the nanoparticles sintered together into a solid pellet. The flow of the experimental procedure is shown in the images in Fig. 4. The sintering experiments were carried out under flowing Argon and Hydrogen to control oxidation of the copper nanoparticles.

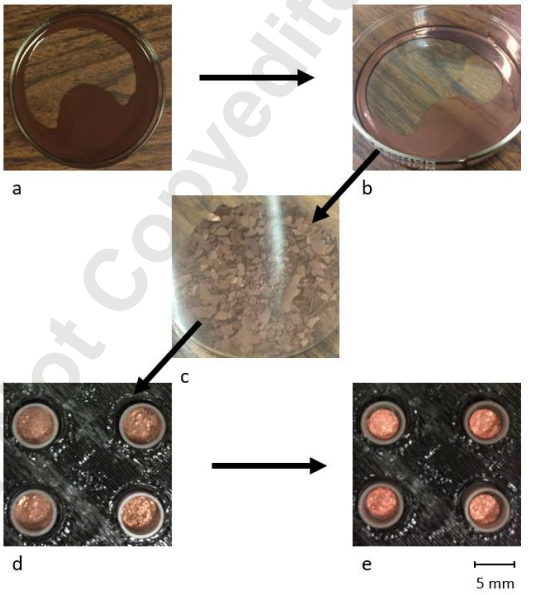


Fig. 4. Experimental procedure. a. Copper nanoparticle ink. b. Dried ink. c. Scraped off dried flakes. d. Pellets in crucible before sintering. e. Pellets in crucible after sintering

SEM images were taken of the flakes before sintering, and the pellets after sintering. These images in Fig. 5, show that before sintering the particles are discrete and can be seen separate from each other. After sintering, the images of the pellets show that necks have formed between the nanoparticles after heating.

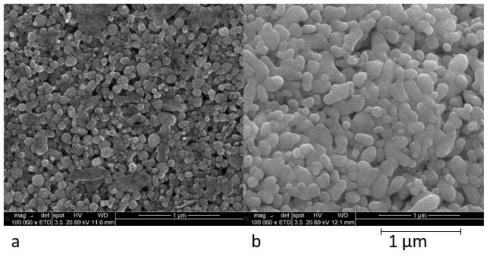


Fig. 5. SEM Images of sintered nanoparticles. a. Before sintering. b. After sintering

Journal of Micro- and Nano-Manufacturing. Received June 07, 2018;
Accepted manuscript posted October 10, 2018. doi:10.1115/1.4041668


Analysis of the sintered copper pellets were carried out after the experiments. The density measurement is calculated as the ratio of mass to volume. The mass was measured using a digital weight scale and the height of the copper nanoparticle pellet in the crucible was measured using a plastic stopper. First, the height of the pellet was calculated as the difference between the height of the stopper when placed in the empty crucible, and the height when placed in the crucible containing the pellet. The volume was then calculated using this measured height and the diameter of the crucible. Similarly, the mass of the pellet was calculated as the difference between the mass of the empty crucible and the mass of the crucible containing the pellet. The initial density of the pellet was calculated from the ratio of mass to volume. The relative density was then calculated based off the measurements taken. This value was calculated using the same equation as was used for the simulation (Eq. 9), where in this case $\rho_o$ corresponds to the initial density of the unsintered pellet and $\rho_i$ is the density after sintering.

The sintering experiments were carried out at 450, 500, 550 and 600˚C. The relative density data at these temperatures were fit to an exponential decay of the form in Eq. 10.

$$\rho_{rel} = K_1 e^{-\frac{K_2}{t+K_3}+K_4} + K_5 \quad (10)$$

Where the K values are best fit constants. The plot of the experiment data points and the best fit curve for the decay in Eq. 10. is shown in Fig. 6. A consolidation of all these plots is shown in Fig. 7. From Fig. 6, it can be seen that sintering is characterized by an initial rate of rapid densification and as the sintering time proceeds the rate of densification approaches a steady state value. Fig. 7 shows that as the temperature increases, the amount of time it takes for the relative density to reach steady state decreases. These curves from the experiments were set against the results from the simulation and the appropriate simulation constants and simulation time calibration constant were calculated. The process of deriving this is discussed in the following sections.

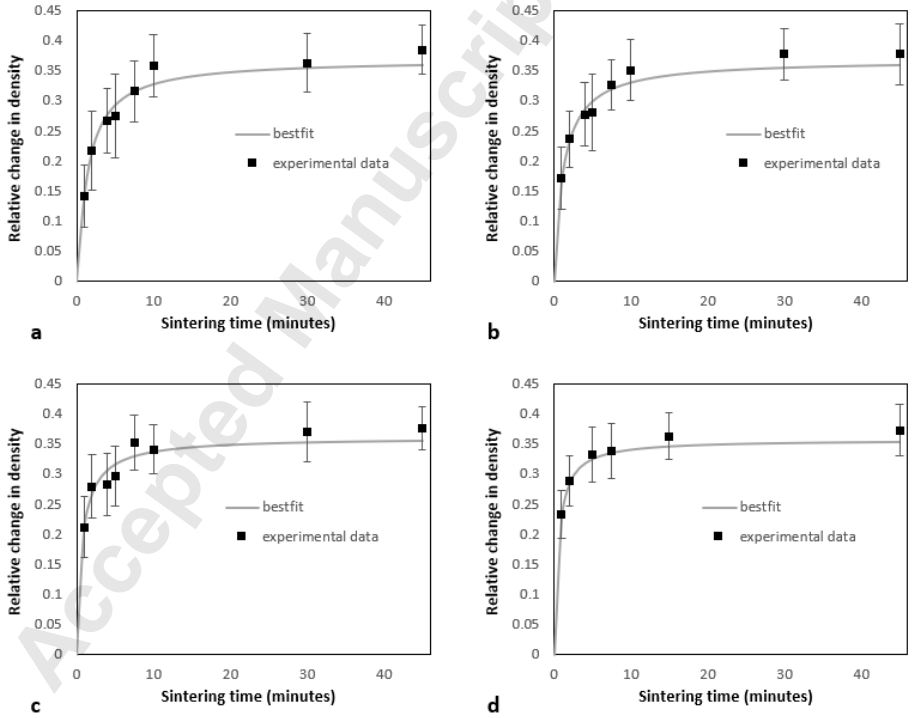


Fig. 6. Experimental data and curve fit at a. 450˚C. b. 500˚C. c. 550˚C. d. 600˚C

Journal of Micro- and Nano-Manufacturing. Received June 07, 2018;
Accepted manuscript posted October 10, 2018. doi:10.1115/1.4041668


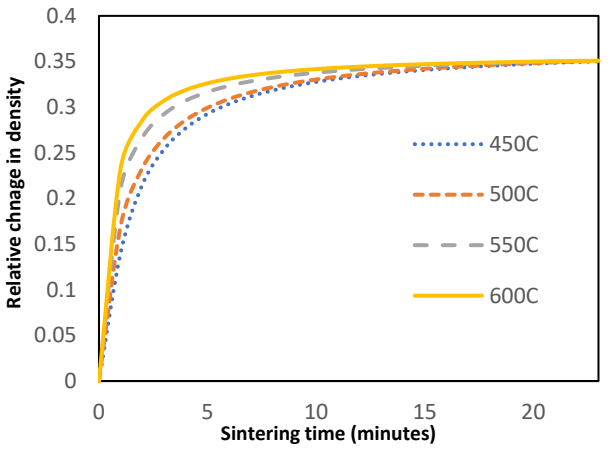


Fig. 7. Consolidation of experiment fit plots

*Experiment and Simulation Sizes*

The goal of carrying out the experiments is to validate and calibrate the simulations. For this calibration, millimeter scale crucibles are used in comparison to micrometer scale simulation beds. This mismatch in size is a result of the infeasibility of applying the same size scales to both the simulation and the experiments. That is, facilities do not exist to conduct experiments on the micron scale and running the simulation on the millimeter scale would require more computational power and time than possible. As such, initial density measurements are taken to make sure that the simulation bed and the experiment bed at the start of sintering are comparable. The procedure for obtaining these density measurements in the experiments are discussed in the experimental procedure section above. The initial density in the simulation bed is determined from the porosity of the simulation bed. The number of pixels in the vapor phase are counted and the pore density is obtained from taking the ratio of porous pixels to the overall number of pixels in the simulation bed. Finally, the initial density for the simulation is calculated by multiplying the percentage of filled pixels (1 – porosity) in the bed with the known density of bulk copper 0.00896 g/mm$^3$. Distributions for the average initial densities from the experiments and simulations are shown in Fig. 8 with lines to indicate the 95% confidence intervals for each distribution. The measurements from the experiments are obtained from an average of 6 measurements taken for each bed. This makes the average density from the experiments follow a normal distribution with an average of 3 mg/mm$^3$ and a standard deviation of 0.06 mg/mm$^3$. The initial density for the simulations follows an unknown distribution. Based off the Central Limit Theorem the approximation can be made that the average of the initial densities from the simulation would follow a normal distribution with a mean of 3.2 mg/mm$^3$ and a standard deviation of 0.1 mg/mm$^3$ (which is the sample standard deviation divided by the square root of the number of points sampled).

A two-tailed p-test was done to test the null hypothesis that both distributions are equal. The p value calculated from this test is 0.074. This value is greater than 0.05, so the null hypothesis cannot be rejected at a 90% confidence level. One reason why the initial densities of the simulations and experiments may differ is due to the precision of measurement. The height measurements of the experiments are done with plastic stoppers which introduce additional errors due to the irregularities in the surface of the stopper. On the other hand, there is no such irregularity in measuring the density of the simulation where the exact pixel height is known. Another reason why the initial densities may differ is due to the polymer coating around the nanoparticles used for the experiments. This creates a mix of materials which is not present in the simulations. Within the uncertainty the initial densities can be said to agree and as such the simulations can be calibrated against the experiments.

Journal of Micro- and Nano-Manufacturing. Received June 07, 2018;
Accepted manuscript posted October 10, 2018. doi:10.1115/1.4041668


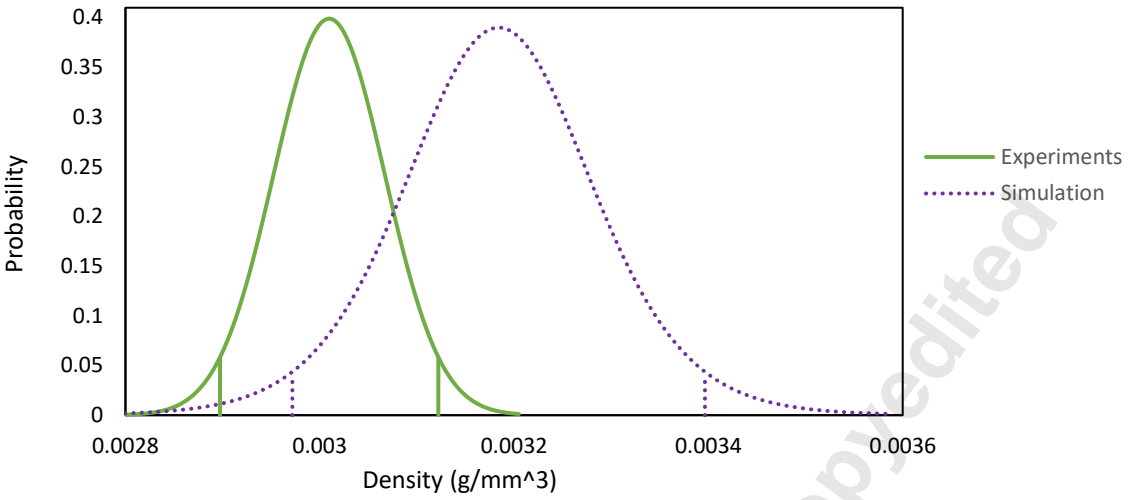


Fig. 8. Distribution of the Average Initial Density of the Simulation and Experiment for 12 Simulation beds and 24 Experiment samples

*Simulation Calibration*

The constants used in the PFM simulation are temperature and time dependent and have simulation units. To map these constants to physical units a time calibration must be done, matching the simulation time in units of timesteps to experimental time in unites of minutes. The simulation was calibrated against experimental data by plotting the percentage change curve from the experiments against that derived from the simulations. The first step for this calibration was arbitrarily changing the values of the simulation constants related to diffusion and energy to get a good comparison between the density curves from the simulations and that of the experiments. After a good rough fit was derived from comparing the simulation data to the experimental data, the simulation time step was calibrated to match experimental sintering time. For the time calibration, the simulation time steps are taken to have a linear correlation with the actual time so that the calibration factor is a constant (A) given in Eq. 11.

$$t_{exp}(min) = \frac{t_{sim}(timesteps)}{A} \tag{11}$$

The calibration factor was determined through a minimization algorithm. This algorithm works by narrowing the possible values of A to a window with upper and lower bounds off by a negligible value of epsilon. The values in this window minimize the total error between the simulation data and the experimental data. The value of A that gives the lowest error is taken as the calibration factor mapping simulation timesteps to experimental time. The results fitting the simulation to experiments are shown in Fig. 9.

Journal of Micro- and Nano-Manufacturing. Received June 07, 2018;
Accepted manuscript posted October 10, 2018. doi:10.1115/1.4041668


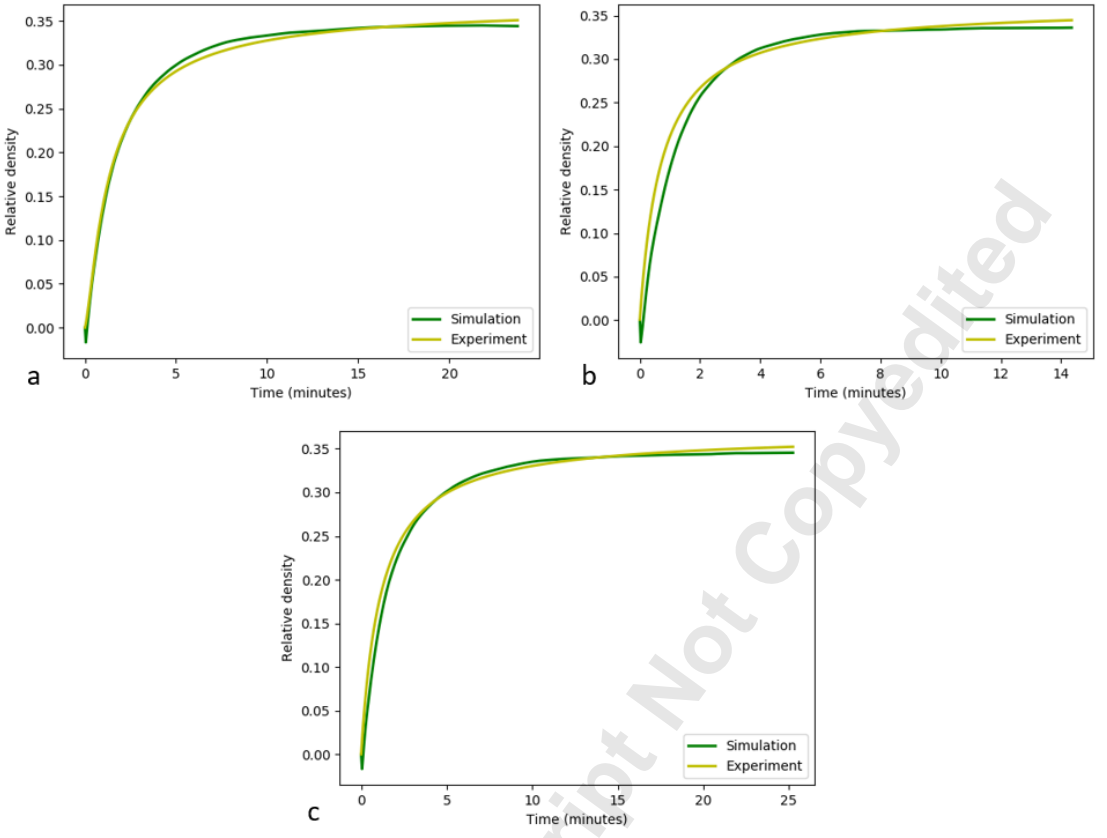


Fig. 9. Comparing experimental fit to simulations for a. 450˚C. b. 500˚C. c. 550˚C

The results for the time calibration values are shown in Table 1. The Table shows the results for the range and averages of the error and time calibration values. The range included in these values, like the error bars in Fig. 3, are a result of carrying out the calibration analysis on different boxes in the center of the simulation bed. The data in Table 1 shows an overall average error of about 9% between the simulation and experiments. The time calibration factor shown in the table has an average of 20% deviation between each temperature.

Table 1. Calibration Results: Time and Error

| | Time Calibration, *A* (timesteps/minute) | | | Error (%) | | |
|---|---|---|---|---|---|---|
| | Minimum | Maximum | Average | Minimum | Maximum | Average |
| 450˚C | 101070 | 388864 | 215319 | 3.22 | 30.14 | 13.54 |
| 500˚C | 57644 | 277293 | 167598 | 3.57 | 10.91 | 7.01 |
| 550˚C | 71110 | 383773 | 250102 | 3.99 | 9.79 | 6.76 |

Journal of Micro- and Nano-Manufacturing. Received June 07, 2018;
Accepted manuscript posted October 10, 2018. doi:10.1115/1.4041668


Once calculated, the simulation diffusion constants were mapped using Eq. 12.

$$D_{sim}\left(\frac{pixels^2}{timesteps}\right) => \frac{D_{sim}A}{60S^2}$$
$$=> D_{actl}\left(\frac{cm^2}{s}\right) \quad (12)$$

Where $D_{sim}$ represents the simulation diffusion coefficients and $D_{actl}$ represents the diffusion coefficients when mapped to the corresponding units in a CGS system. A is the time calibration constant in Eq. 11 having units of timesteps/minute and S is the size calibration constant. S here is set as 944822 pixels/cm. The values used for the diffusion constants in the simulation where mapped to physical units and are shown in Table 2. For this study surface, grain boundary and volume diffusion coefficients are assumed to follow the ratio 1000:100:1 [24,25] respectively. As these constants are the final constants derived from the best fit between the experiments and the simulation, they represent sintering simulation constants for copper at the temperatures stated in the table.

Table 2. Calibration Results: Diffusion constants

| | Surface Diffusion coefficients (cm^2/s) | |
|---|---|---|
| | Average | Uncertainty |
| 450˚C | 2E-07 | 1E-07 |
| 500˚C | 2.2E-07 | 7.9E-08 |
| 550˚C | 3E-07 | 1E-07 |

As of this point there has been no experimentally determined surface diffusion coefficients for copper nanoparticles to compare against the constants in Table 2. Bonzel and Gjostein [26] found that at 500˚C the surface diffusion coefficient of bulk copper is 1.91E-07 $cm^2/s$. This value falls within the same order of magnitude as the value obtained from the simulations, which is further validation of the model.

*Two-by-Two Micrometer Bed*

One of the goals for the model described in this paper is to be able to apply it to over a hundred particles. To this end the simulation was applied to a two-by-two micrometer bed. The configuration of this bed was determined using the same bed generation tool as described earlier, and the PFM simulation was run on this bed. The two-by-two micrometer bed corresponds to 134 particles with diameters ranging between 118 to 572 nm. The bed was created using the same particle size distribution as used for the one-by-one micrometer bed. The two-by-two micrometer bed had a simulation box size of 286 by 282 pixels in the x-y plane and 98 pixels in the z. With a 140 core cluster the simulation took 48 hours to run to 220,000 time steps, and 52 hours to run to 2,030,000 time steps in a 1440 core cluster. The results from the simulation are shown in Fig. 10. As was the case with the one-by-one bed, these images show a similar rate of rapid initial neck formation and a slower rate of densification and shrinkages as sintering proceeds.

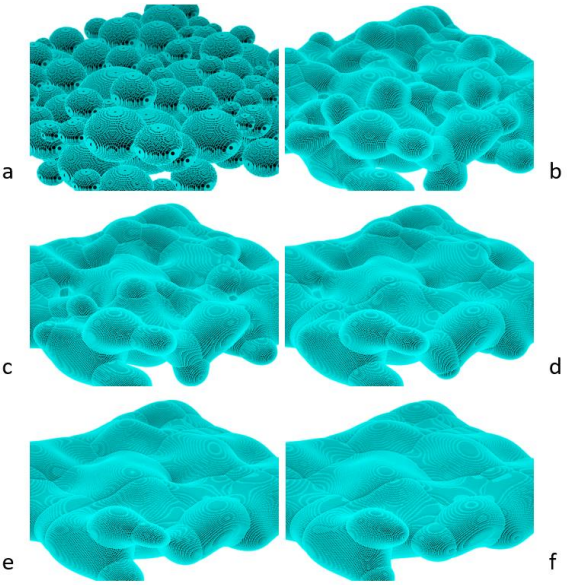


Fig. 10. The evolution of a two by two micrometer bed with 134 particles. a. Initial b. 200000 timesteps (5.1 hrs.) c. 600000 timesteps (15 hrs.) d. 1000000 timesteps (26 hrs.) e. 1500000 timesteps (38 hrs.) f. 2000000 timesteps (51 hrs.)

Journal of Micro- and Nano-Manufacturing. Received June 07, 2018;
Accepted manuscript posted October 10, 2018. doi:10.1115/1.4041668


Analysis done on this bed and shown in Fig. 11 quantitatively confirms that the densification is similar to that seen in the one-by-one micrometer bed.

The plots in Fig. 11 show two density curves. The density curve in the dashed line is a prediction from scaling the results of a one-by-one micrometer bed by a factor of the areal magnification between both beds. The average error between the prediction and the actual density curve derived from the analysis of the beds is 12% which is smaller than the uncertainty in these curves. This error value shows a good degree of accuracy in scaling up the results using analysis of the smaller bed. The significance of this test is to show the viability of extrapolating results from one-by-one micrometer beds for larger beds which are more computationally expensive to run.

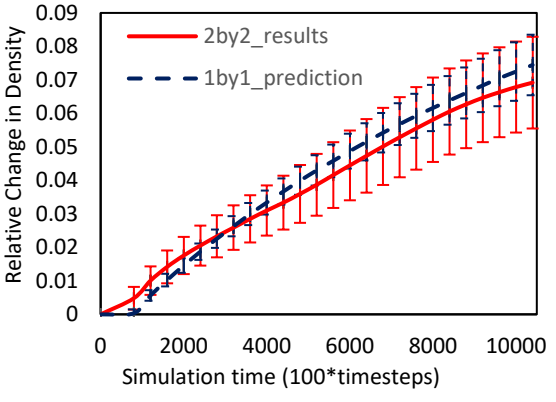


Fig. 11. Relative change in density curve derived from data analysis done on a 2-by-2 micrometer bed and the prediction from a 1-by1 micrometer bed.

## CONCLUSION

In this paper a Phase Field Modelling (PFM) approach is used to simulate the sintering of particles in a one-by-one micrometer bed. The simulations presented here are unique in that they are applied to 3D bed scale simulations using clusters which can be extended to hundreds of particles. The validity of expanding this simulation is tested against a larger two-by-two micrometer bed containing 134 particles. Additionally, a data analysis package was created that measures the relative density change in each bed. Experiments were also performed with a furnace. The experimental data shows that after 10 minutes of heating at 450˚C the density value starts to reach the maximum steady state value. As heating temperature increases, the amount of time the nanoparticles take to reach steady state decreases. The densification curves obtained from the experimental data are calibrated to match sintering simulation results and it is seen that the simulation trend is in good agreement with the experimental data. These comparisons between the simulation and experiments gave a calibration factor mapping the simulation timestep to sintering time in minutes. The time calibration factor derived was then used to map the diffusion constants from simulation units to physical units and the resulting surface diffusion constant showed good agreement with experimental data.

For full reliability in this model the uncertainty in the sintering process caused by variations of the sizes and locations of nanoparticles in the bed must be quantified. As shown in the results derived from changing the position of the analysis box, there is a significant amount of uncertainty that comes with the configuration of the particles in the bed. To completely quantify this uncertainty, different simulation beds have to be tested to determine the changes in calibration constants and rate of densification with changing the initial configuration of the bed.

In conclusion, the low percentage error between the simulation and the experiments done on the copper nanoparticles give qualitative evidence that this model is indeed valid for calculating the rate of densification in nanoparticle sintering.

## ACKNOWLEDGEMENTS

This study was made possible through the Supercomputing resources of the Texas Advanced Computing Center. The authors would also like to thank NXP Semiconductors for the financial support provided. This material is based upon work supported by the National Science Foundation under Grant No. 1728313.

## REFERENCES

[1] Design Guidelines: Laser Sintering (LS), (n.d.). Retrieved June 28, 2017, from https://www.stratasysdirect.com/resources/laser-sintering/.
[2] B. Sager, D. Rosen, Stereolithography Process Resolution, Georgia Institute of Technology, (n.d.).
[3] N. K. Roy, C. S. Foong, M. A. Cullinan, Design of a Micro-scale Selective Laser Sintering System, 2016 Annual International Solid Freeform Fabrication Symposium, (2016).
[4] N. Roy, A. Yuksel, M. Cullinan, Design and Modeling of a Microscale Selective Laser Sintering System, ASME 2016 11th International Manufacturing Science and Engineering Conference, (2016).

[5] N. Roy, O. Dibua, C. S. Foong, M. Cullinan, Preliminary Results on the Fabrication of Interconnect Structures Using Microscale Selective Laser Sintering, Proceedings of the ASME 2017 International Technical Conference and Exhibition on Packaging and Integration of Electronic and Photonic Microsystems, (2017).

[6] C. Nelson, K. McAlea, D. Gray, 1995, Improvements in SLS Part Accuracy, Annual International Solid Freeform Fabrication Symposium, (1995) 159-169.

[7] L. Dong, A. Makradi, S. Ahzi, Y. Remond, 2009, Three-dimensional transient finite element analysis of the selective laser sintering process, Journal of Materials Processing Technology, 209 (2009) 700-706.

[8] D. Moser, M. Cullinan, J. Murthy, Particle-Scale Melt Modeling of the Selective Laser Melting Process, 2016 Annual International Solid Freeform Fabrication Symposium, (2016) 247-256.

[9] D. Moser, S. Fish, J. Beaman, J. Murthy, Multi-Layer Computational Modeling of Selective Laser Sintering Processes, ASME 2014 International Mechanical Engineering Congress and Exposition, 2A (2014) V02AT02A008- V02AT02A018.

[10] S. H. Ko, C. P. Grigoropoulos, The Solid-State Neck Growth Mechanisms in Low Energy Laser Sintering of Gold Nanoparticles: A Molecular Dynamics Simulation Study, Journal of Heat Transfer, 130 (2008) 092404-1 – 092404-7.

[11] L. Ding, L. R. Davidchack, J. Pan, A molecular dynamics study of sintering between nanoparticles, Computational Materials Science, 45 (2009) 247-256.

[12] B. Cheng, H. W. A. Ngan, The Sintering and Densification Behavior of Many Copper Nanoparticles: A molecular Dynamics Study, Computational Materials Science, 74 (2013) 1-11.

[13] J. Rojek, S. Nosewicz, K. Pietrzak, M. Chmielewski, D. Kalinski, Modelling of powder sintering using the discrete element method, Computer Methods in Mechanics, (2011).

[14] U. Y. Wang, Computer Modeling and Simulation of Solid-State Sintering: A Phase Field Approach, Acta Materialia, 54 (2006) 953-961.

[15] K. Shinagawa, Simulation of Grain Growth and Sintering Process by Combined Phase-Field/Discrete Element Method, Acta Materialia, 66 (2014) 360-369.

[16] V. Kumar, Simulations and modeling of unequal sized particles sintering, Diss. The University of Utah (2011).

[17] N. Moelans, B. Blanpain, P. Wollants, An introduction to phase-field modeling of microstructure evolution, Computer Coupling of Phase Diagrams and Thermochemistry, 32 (2008) 268-294.

[18] K. Chockalingam, V. G. Kouznetsova, O. van der Sluis, M. G. D. Geers, 2D Phase field modeling of sintering of silver nanoparticles, Comput. Methods Appl. Mech. Engrg, (2016).

[19] J. W. Cahn, J. E. Hilliard, Free Energy of a Nonuniform System. I. Interfacial Free Energy, The Journal of Chemical Physics, 28 (1958) 258-267.

[20] J. W. Cahn, On Spinodal Decomposition, Acta Metallurgica, 9 (1961) 81-87.

[21] V. L. Ginzburgh, L. D. Landau, On the theory of superconductivity, Soviet Physics – Journal of experimental and Theoretical Physics, 20 (1950) 1064-1082.

[22] A. Yuksel, M. Cullinan, Modeling of nanoparticle agglomeration and powder bed formation in microscale selective laser sintering systems, Additive Manufacturing, 12 (2016) 204-215.

[23] n.d. "CI-005_Data_Sheet_2017," Intrinsiq Materials.

[24] J. Deng, A Phase Field Model of Sintering with Direction-Dependent Diffusion, Materials transactions, 53 (2012) 385-389.

[25] D. Zhang, G. Weng, S. Gong, D. Zhou, The Kinetics of Initial Stage in Sintering Process of $BaTiO_3$-based PTCR ceramics and its computer simulation, Materials Science & Engineering B, 99 (2003) 88-92.

[26] K. Hoehne, R. Sizmann, Volume and Surface Self-Diffusion Measurements on Copper by Thermal Surface Smoothing, Physica Status Solidi, 5 (1971) 577-589.

List of Figures



List of Tables